J. Fluid Mech. (2025), *vol.* 1021, A42, doi:10.1017/jfm.2025.10729

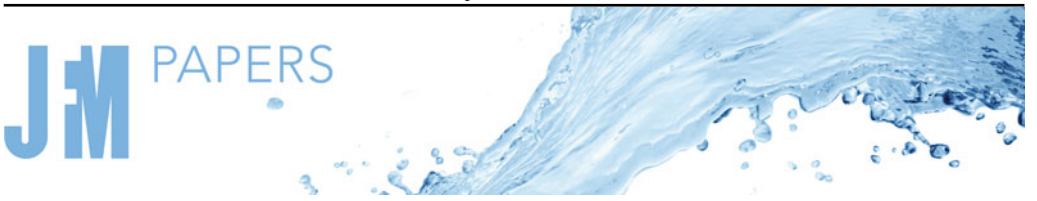

Yield-stress fluid mixing: localisation mechanisms and regime transitions

Mohammad Reza Daneshvar Garmroodi[1] **and Ida Karimfazli**[1]

[1]Department of Mechanical, Industrial and Aerospace Engineering, Concordia University, 1515 St.Catherine W., Montreal, QC H3G 2W1, Canada

Corresponding author: Ida Karimfazli, ida.karimfazli@gmail.com

(Received 29 October 2024; revised 6 September 2025; accepted 12 September 2025)

We explore the mechanisms and regimes of mixing in yield-stress fluids by simulating the stirring of an infinite, two-dimensional domain filled with a Bingham fluid. A cylindrical stirrer moves along a circular path at constant speed, with the path radius fixed at twice the stirrer diameter; the domain is initially quiescent and marked by a passive dye in the lower half. We first examine the mixing process in Newtonian fluids, identifying three key mechanisms: interface stretching and folding around the stirrer's path, diffusion across streamlines and dye advection and interface stretching due to vortex shedding. Introducing yield stress leads to notable mixing localisation, manifesting through three mechanisms: advection of vortices within a finite distance of the stirrer, vortex entrapment near the stirrer and complete suppression of vortex shedding at high yield stresses. Based on these mechanisms, we classify three distinct mixing regimes: (i) regime SE, where shed vortices escape the central region, (ii) regime ST, where shed vortices remain trapped near the stirrer and (iii) regime NS, where no vortex shedding occurs. These regimes are quantitatively distinguished through spectral analysis of energy oscillations, revealing transitions and the critical Bingham and Reynolds numbers. The transitions are captured through effective Reynolds numbers, supporting the hypothesis that mixing regime transitions in yield-stress fluids share fundamental characteristics with bluff-body flow dynamics. The findings provide a mechanistic framework for understanding and predicting mixing behaviours in yield-stress fluids, suggesting that the localisation mechanisms and mixing regimes observed here are archetypal for stirred-tank applications.

Key words: complex fluids, laminar mixing, plastic materials

1. Introduction

Mixing is ubiquitous in both natural and industrial environments. Applications span a vast range of Reynolds numbers and length scales (see figure 1 in Ottino 1990 for

illustration). From the coffee we drink, household cleaning products and oil extraction to the human digestive system and pharmaceutical production, various materials undergo mixing processes daily.

Despite its prevalence, mixing remains one of the more challenging paradigms in engineering to systematically define, frame and understand (Spencer & Wiley 1951; Ottino 1990; Villermaux 2019). In the simplest context, mixing entails the homogenisation of a passive tracer (level-1); however, it can be more intricately tied to the flow dynamics, as when rheology depends on tracer concentration (level-2), or chemical reactions occur during the process (level-3) (Dimotakis 2005).

A significant body of literature focuses on level-1 mixing, i.e. mixing of a passive dye in fluid. Even within this limited scope, the parameter space is extensive: mixing may be in line, active or passive, or take place in a stirred tank. Factors like domain geometry, impeller shape, size, position, stirring protocol and speed all influence mixing behaviour. Additionally, fluid rheology plays a critical role. Given the vast range of parameters and the complexity of the problem, most studies have focused on Newtonian fluids, and mixing remains an active research area (see Warhaft 2000; Peltier & Caulfield 2003; Wunsch & Ferrari 2004; Caulfield 2021 and references therein).

Many fluids in polymer processing, food engineering, bioengineering, physiology and chemical engineering are non-Newtonian, with a subset exhibiting yield stress, such as polymeric gels, muds, paints and cosmetics. Yield-stress fluids are highly viscous materials that flow only when the applied shear stress exceeds a threshold known as the yield stress (Balmforth, Frigaard & Ovarlez 2014; Coussot 2014; Bonn *et al.* 2017). It was recognised early on that turbulent mixing in these fluids is economically and technologically impractical. Spencer & Wiley (1951) proposed streamline mixing, achieved by continuously deforming the fluid to (*a*) increase the surface area of the interface and (*b*) distribute it throughout the material volume. With few exceptions (Derksen 2013; Daneshvar Garmroodi & Karimfazli 2024), studies of mixing in yield-stress fluids focus on the mixing of passive dyes.

Initial efforts to understand mixing of non-Newtonian fluids were dedicated to establishing a relationship between impeller speed (in stirred tanks) and the fluid shear rate. According to Metzner & Otto (1957), mixing flows of non-Newtonian fluids were qualitatively understood at best in the 1950s, a sentiment that remained accurate for decades. One of the first studies on mixing yield-stress fluids was conducted by Solomon *et al.* (1981), who experimentally identified the well-mixed regions in Xanthan gum and Carbopol solutions in stirred tanks. The coexistence of flowing and stagnant regions presented a challenge, as the latter remained unmixed. Whitcomb & Macosko (1978) introduced the term cavern to describe the well-mixed region where the fluid was yielded.

Although debate remains regarding the existence of a true yield stress and optimal measurement methods (Barnes 1999; Divoux, Barentin & Manneville 2011; Dinkgreve *et al.* 2016), viscoplastic models are widely used to analyse and predict flows of yield-stress fluids (Mitsoulis & Tsamopoulos 2017). These models consider the fluid rigid below the yield stress and a flow with shear rate-dependent viscosity when the yield stress is exceeded.

Solomon *et al.* (1981) used viscoplastic models and a yield criterion to estimate cavern size by assuming it to be spherical. Subsequent studies explored various impellers and developed cavern size estimates based on different simplified geometries; see, for example, Galindo *et al.* (1996), Tanguy *et al.* (1996), Amanullah, Hjorth & Nienow (1998), Pakzad *et al.* (2013), Sossa-Echeverria & Taghipour (2015) and Ameur (2020). Generally, a yield stress and shear-thinning viscosity reduce the mixing rate and extent and the cavern

size. However, a mechanistic understanding of how the flow dynamics and mixing are interlinked, especially with respect to rheological parameters, remains elusive.

Seminal works by Aref (1984) and Ottino (1989) demonstrated the role of chaotic flows in effective mixing, emphasising the necessity of three-dimensional or transient two-dimensional flows. A parallel branch of research has since modelled mixing by analysing dynamical systems, with a primary focus on chaotic mixing in two-dimensional time-periodic flows; for an overview of studies of Newtonian fluids, see Aref *et al.* (2017).

Niederkorn & Ottino (1994) numerically investigated chaotic advection in journal bearing flows for shear-thinning fluids, examining tracer advection, periodic points, stretching along unstable manifolds and stretching rate of fluid elements. They found that shear-thinning viscosity decreases the amount of stretching. Fan, Phan-Thien & Tanner (2001) studied advective mixing of viscoplastic fluids between eccentric cylinders, showing that tracer coverage may depend on initial tracer position, and chaotic advection can be achieved through alternating cylinder rotations. Their results highlight qualitative transitions but do not predict when such transitions will occur.

Experimental studies by Wendell *et al.* (2013) explored mixing in a rotating tank filled with a yield-stress fluid stirred by cylindrical rods rotating with constant angular velocity in an eggbeater configuration. Higher period ratios and lower yield stresses enhanced mixing, although mixing efficiency decreased in resonance conditions. The intermittent yielding and unyielding near the tank wall was hypothesised to explain the decreased mixing of yield-stress fluids. Further experiments by Boujlel *et al.* (2016) in the same set-up measured mixing rate using dye concentration variance, showing that mixing consists of rapid stretching and folding followed by slower diffusion-dominated mixing. They concluded that mixing rate is proportional to the volume of highly sheared fluid during each rod rotation.

In summary, while the qualitative impact of yield stress on mixing is understood – yield stress limits cavern size and filament stretching, thus decreasing mixing rate – a mechanistic description connecting the fluid dynamics to transitions in yield-stress fluid mixing remains absent. Decades after Niederkorn & Ottino (1994), design procedures still rely heavily on empiricism with a limited fundamental understanding of the fluid mechanics (see Paul *et al.* 2004; Uhl 2012).

The primary objective of this manuscript is to identify and elucidate the mechanisms behind different mixing regimes and localisation in yield-stress fluids within a periodically stirred domain. We consider the simplest and most common viscoplastic model, the Bingham model, thus neglecting the thixotropy and elasticity typically associated with real yield-stress fluids. Potential influences of dye concentration on fluid properties and density are similarly neglected. We also adopt a minimalistic stirrer geometry and stirring strategy to avoid the added complexity of geometric effects and to isolate the roles of yield stress and localisation. We consider an infinite two-dimensional domain filled with a quiescent viscoplastic fluid stirred by a cylinder moving at constant speed along a circular path. By exploring a range of mixing speeds and yield stresses, we aim to characterise the flow and the mixing dynamics and establish a mechanistic link between them.

This problem is closely related to the classical flow past a circular cylinder. Over the past few decades, numerous studies have examined the flow of yield-stress fluids around a cylinder, either being drawn through the fluid or moving due to buoyancy (referred to as the resistance and mobility problems, respectively Putz & Frigaard 2010). These studies typically focus on regimes where inertial effects are negligible and vortex shedding does not occur. Numerical, experimental and analytical results have been developed for predicting the terminal velocity, drag forces and the critical yield stress beyond

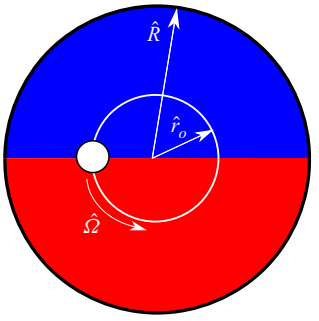

Figure 1. Schematic of the domain geometry and initial conditions. The solid white line indicates the stirrer's path. The red and blue colours indicate the dyed and dye-free regions. Note that the figure is not to scale.

which motion is arrested (see, e.g. Tokpavi *et al.* 2008, 2009; Wachs & Frigaard 2016; Chaparian & Frigaard 2017*a*,*b*). However, parameter regimes characterised by weak inertia or dominated by large unyielded regions are not conducive to strong advective mixing.

The parameter space considered in this study is therefore complementary to the existing body of literature. We explore a broad range of Reynolds numbers within the laminar regime and yield-stress values away from the critical limit, where unyielded zones dominate and regularised numerical models are less accurate. This allows us to capture the mixing dynamics that involves vortex shedding and yield-stress-driven localisation.

The remainder of this paper is organised as follows: § 2 presents the model problem, governing equations and numerical methods. Section 3 discusses the flow dynamics and mixing regimes using representative cases and maps out mixing mechanisms and flow regimes at different mixing speeds and yield stresses. Finally, § 4 summarises our findings.

2. Problem set-up

2.1. *Model problem*

We investigate the stirring of a viscoplastic fluid (VPF) using a circular stirrer of diameter $\hat{d}_s$, which moves at a constant speed ($\hat{r}_o\hat{\Omega}$) along a circular trajectory with radius $\hat{r}_o = c\hat{d}_s$ (solid white line in figure 1). Here, c is the dimensionless stirring radius, fixed at $c = 2$ in this study, and $\hat{\Omega} > 0$ denotes the angular velocity of the stirrer. Dimensional quantities are denoted by a $\hat{\cdot}$ symbol, while dimensionless quantities are written without it. To simulate mixing in an infinite domain, we employ a circular computational domain with a radius $\hat{R} \gg \hat{r}_o$ ($\hat{R} = 34\hat{r}_o$), ensuring minimal boundary effects due to the domain's sufficiently large size. To monitor mixing, the fluid in the bottom half of the domain is marked with a passive dye (shown in red in figure 1), where $\alpha = 1$, while the rest of the fluid is dye free (shown in blue), with $\alpha = 0$. The no-slip boundary condition is imposed on the walls of both the vessel and the stirrer.

The fluid is modelled using the Bingham model. The dimensionless form of the constitutive equation is given by

$$\begin{cases} \boldsymbol{\tau} = \left(\dfrac{Bn}{\dot{\gamma}} + 1\right)\dot{\boldsymbol{\gamma}} & \text{if} \quad \tau \geqslant Bn, \\ \dot{\boldsymbol{\gamma}} = 0 & \text{if} \quad \tau < Bn, \end{cases} \tag{2.1}$$

Dimensionless group	Definition	Value/Range
Reynolds (Re)	$\hat{\rho}\hat{\Omega}\hat{r}_o^2/\hat{\mu}$	$50-300$
Péclet (Pe)	$\hat{\Omega}\hat{r}_o^2/\hat{D}$	10^3
Bingham (Bn)	$\hat{\tau}_y/\hat{\mu}\hat{\Omega}$	$0-10^2$
Stirring radius (c)	$\hat{r}_o/\hat{d}_s$	2

Table 1. Dimensionless groups governing the model problem.

where $\boldsymbol{\tau}$ and $\dot{\boldsymbol{\gamma}}$ are the deviatoric stress and rate of strain tensors, respectively, and

$$\tau = \sqrt{\frac{1}{2}\,\boldsymbol{\tau}:\boldsymbol{\tau}} \quad \text{and} \quad \dot{\gamma} = \sqrt{\frac{1}{2}\,\dot{\boldsymbol{\gamma}}:\dot{\boldsymbol{\gamma}}} \tag{2.2}$$

represent second invariants of these tensors. The Bingham number, Bn, is defined by

$$Bn = \frac{\hat{\tau}_y}{\hat{\mu}\hat{\Omega}}, \tag{2.3}$$

where τ_y and $\hat{\mu}$ are the fluid's yield stress and plastic viscosity.

The flow is governed by the Cauchy's equations of motion and continuity while the dye concentration is described by an advection–diffusion equation

$$\begin{gathered}\frac{\partial \boldsymbol{u}}{\partial t} + \boldsymbol{u}\cdot\nabla\boldsymbol{u} + \nabla P = \frac{1}{Re}\nabla\cdot\boldsymbol{\tau} \\ \nabla\cdot\boldsymbol{u} = 0 \\ \frac{\partial \alpha}{\partial t} + \nabla\cdot(\boldsymbol{u}\alpha) = \frac{1}{Pe}\nabla^2\alpha.\end{gathered} \tag{2.4}$$

Here, $\boldsymbol{u}$ and P are the dimensionless velocity and pressure, respectively. The characteristic scales for length, time, velocity, shear stress and pressure are $\hat{r}_o$, $\hat{\Omega}^{-1}$, $\hat{r}_o\hat{\Omega}$, $\hat{\mu}\hat{\Omega}$ and $\hat{\rho}\hat{r}_o^2\hat{\Omega}^2$, where $\hat{\rho}$ is the density of the fluid. Results, however, are presented in terms of the stirrer's period, $\hat{T}_{stirrer} = 2\pi/\hat{\Omega}$

$$T = \frac{\hat{t}}{\hat{T}_{stirrer}} = \frac{t}{2\pi}. \tag{2.5}$$

The Reynolds (Re) and Péclet numbers (Pe) are defined as

$$Re = \frac{\hat{\rho}\hat{\Omega}\hat{r}_o^2}{\hat{\mu}}, \tag{2.6}$$

$$Pe = \frac{\hat{\Omega}\hat{r}_o^2}{\hat{D}_m}, \tag{2.7}$$

where $\hat{D}_m$ is the diffusion coefficient of dye. In this study, Péclet number is held constant at $Pe = 10^3$.

Definitions and ranges of the relevant dimensionless groups are summarised in table 1.

To characterise the rate of mixing, a normalised variance of the dye, $\sigma^2_{R_{sd}}$, is defined over a circular subdomain $A_{R_{sd}}$ of radius R_{sd} that is concentric with the stirrer's path

$$\sigma^2_{R_{sd}} = \frac{1}{A_{R_{sd}}}\int_{A_{R_{sd}}}\left(1-\frac{\alpha}{\bar{\alpha}}\right)^2 \mathrm{d}A. \tag{2.8}$$

Here, $\bar{\alpha}$ is the average dye concentration over the subdomain, for all R_{sd}. For given values of the governing dimensionless parameters, R_{sd} is chosen to ensure the subdomain captures the region where dye concentration is affected by the stirring (within the timeframe of interest).

To quantify the kinetic energy, KE is defined as

$$KE = \sqrt{\int_A |\boldsymbol{u}|^2 \mathrm{d}A}, \tag{2.9}$$

where KE is the kinetic energy, $|\boldsymbol{u}|$ is the speed and A represents the flow domain.

2.2. *Numerical method*

OpenFOAM – Open Source Computational Fluid Dynamics (2004) version 6 was used for numerical simulations. The *twoLiquidMixingFoam* solver, which employs the PIMPLE (PISO–SIMPLE) algorithm, which combines PISO (Pressure-Implicit with Splitting of Operators) and SIMPLE (Semi-Implicit Method for Pressure-Linked Equations) algorithms, to decouple pressure and velocity in the governing equations, was utilised. For temporal discretisation, we applied the second-order Crank–Nicolson scheme. The viscous terms are discretised using a second-order centred scheme, while the convective (inertial) terms are treated with a second-order upwind-biased scheme. The second-order vanLeer scheme is used for the concentration field transport. Adaptive time stepping was implemented using a constant Courant–Friedrichs–Lewy number (set to 0.05 to ensure sufficient accuracy in transient results).

In this study, we adopt a modified version of the bi-viscosity model originally developed by Tanner & Milthorpe (1983)

$$\boldsymbol{\tau}(\dot{\gamma}) = \begin{cases} \left(1 + \dfrac{Bn}{\dot{\gamma}_{cr}}\right)\dot{\boldsymbol{\gamma}} & \text{if} \quad \dot{\gamma} \leqslant \dot{\gamma}_{cr}, \\ \left(1 + \dfrac{Bn}{\dot{\gamma}}\right)\dot{\boldsymbol{\gamma}} & \text{if} \quad \dot{\gamma} > \dot{\gamma}_{cr}. \end{cases} \tag{2.10}$$

Here, $\dot{\gamma}_{cr}$ is the critical strain rate. Because the numerical scheme involves regularisation, the accuracy of predictions for the unyielded regions decreases significantly at high Bn (Frigaard & Nouar 2005; Ahmadi, Olleik & Karimfazli 2021), making the scheme unsuitable for exploring the limit behaviour in that regime. For the parameter ranges considered here, $\dot{\gamma}_{cr}$ is chosen so that the error in the average radius of the yielded regions remains safely below 1 %; specifically, $\dot{\gamma}_{cr} = \hat{\dot{\gamma}}_{cr}/\hat{\Omega} = 10^{-4}$.

To verify grid independence, five different mesh sizes were tested. Figure 2 shows the evolution of normalised variance and velocity norm, along with the corresponding relative errors for different mesh sizes. The finest mesh (1.3×10^5) was used to estimate the relative error. For the remainder of the simulations, we used a mesh size of 8×10^4, which resulted in a relative error of less than 1 % for both the normalised variance and velocity norm. Further details on the benchmarking and validation of the numerical solver can be found in Daneshvar Garmroodi & Karimfazli (2024).

3. Results and discussion

3.1. *The Newtonian limit*

Figure 3 shows snapshots of dye concentration in a Newtonian fluid ($Bn = 0$) at $Re = 100$. To facilitate the illustration of concentration development, the snapshots show subdomains of different radii (indicated as R_{sd} in the captions). The white and grey lines show

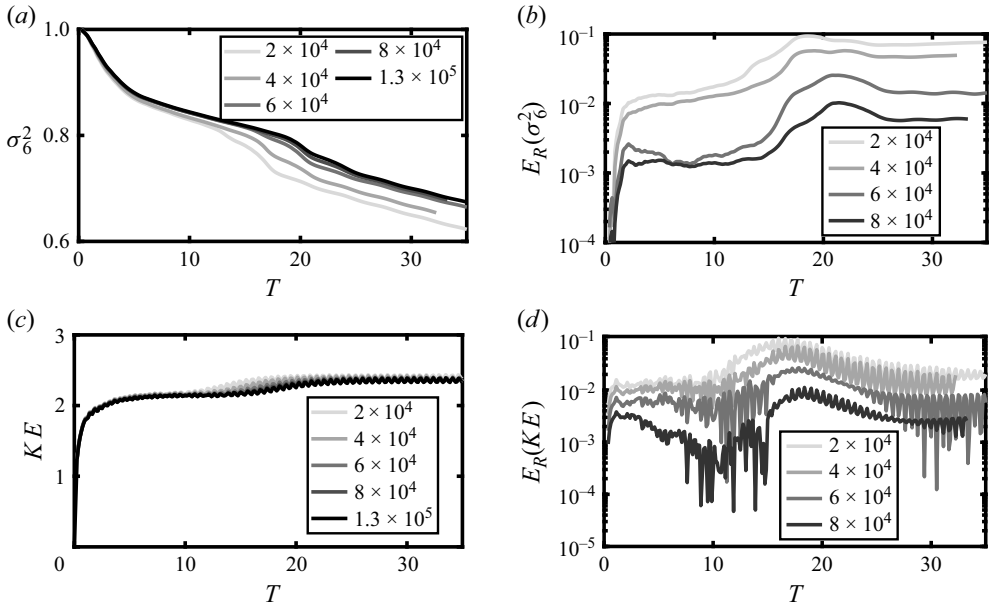

Figure 2. Time evolution of (a) normalised variance of dye concentration for different mesh sizes, (b) relative error in dye concentration variance, $E_R(\sigma_6^2) = (\sigma_6^2 - \sigma^2_{6,\ 1.3\times10^5})/(\sigma^2_{6,\ 1.3\times10^5})$, ($c$) kinetic energy for different mesh sizes and (d) relative error in kinetic energy, $E_R(KE) = (KE - KE_{1.3\times10^5})/(KE_{1.3\times10^5})$, for $Re = 300$ and $Bn = 2$.

the stirrer's path and the streamlines, respectively. A normalised variance of the dye concentration, σ_{20}^2, is shown in figure 3(g). The markers in figure 3(g) indicate the time instances of the snapshots.

When stirring begins, the stirrer crosses the dye interface periodically, stretching and folding it (see, e.g. figures 3a and 3b). This action creates a striated pattern near the stirrer's path, from hereon referred to as the 'central region'. The stretched interface and thin striations promote local diffusion. As a result, mixing proceeds rapidly during this stage, characterised by a sharp decline in σ_{20}^2 (see figure 3g). Mixing slows down once the dye concentration becomes nearly uniform along the stirrer's path ($T \approx 10$; see figure 3c).

For $10 \lesssim T \lesssim 20$, the dye concentration appears approximately axisymmetric within the central region, and mixing is temporarily dominated by radial diffusion across the streamlines within this region and across the boundary of this region (figure 3d). A well-mixed subdomain, where the dye concentration is $\alpha \approx 0.5$, thus develops in the central region. However, this region is not quiescent, as the flow is not axisymmetric. Figure 3(e) shows that the well-mixed region is slowly advected by the flow, following an approximately helical trajectory. Consequently, the dye interface is brought back into the stirrer's path, where it is once again stretched and folded (figure 3f). The acceleration of mixing during this stage is congruent with the downward concavity of σ_{20}^2 for $T \gtrsim 20$ (figure 3g).

Another mechanism contributing to mixing during this phase ($T \gtrsim 20$) is the extensive stretching of the interface beyond the central region (see figure 3f). As the well-mixed region drifts away from the centre, interface stretching extends beyond the stirrer's direct influence. This contributes to the sharp decay rates observed in σ_{20}^2 during this period ($T \gtrsim 20$).

The development of the dye concentration is governed by the momentum balance in the flow field; i.e. the coupling between the dye concentration and momentum transfer is one

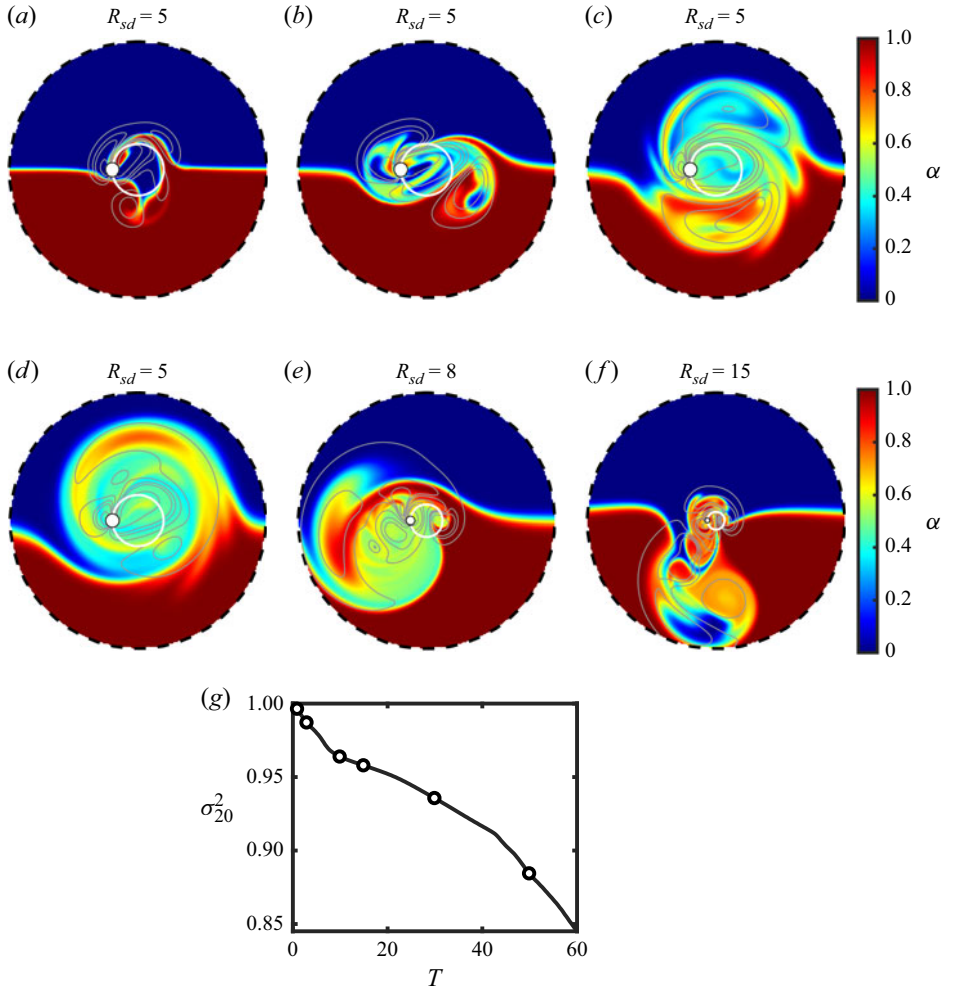

Figure 3. (*a–f*) Snapshots of the dye concentration field in a Newtonian fluid, $Bn = 0$, $Re = 100$, at times $T = 1$, 3, 10, 15, 30 and 50. The white circle marks the stirrer's path, while grey lines represent the streamlines. The radius of the field of view is provided in the caption. (*g*) Time evolution of the normalised variance, with circular markers indicating the time instances of the snapshots in (*a–f*).

way because the rheology and density are independent of the dye concentration. Figure 4 illustrates the development of the vorticity field in Newtonian fluids at $Re = 100$, at the same time instances as figure 3. Similar to figure 3, the white circular line is the stirrer's path and the grey lines are streamlines. To facilitate the illustration of the vorticity field, a scaled vorticity magnitude (ζ) is defined as follows:

$$\zeta = \begin{cases} \log(\omega_z + 1) & \text{if} \quad \omega_z \geqslant 0, \\ -\log(|\omega_z| + 1) & \text{if} \quad \omega_z < 0. \end{cases} \tag{3.1}$$

Note that ζ retains the sign of ω_z; i.e. positive and negative ζ indicate counter-clockwise (CCW) and clockwise (CW) rotation, respectively.

When stirring starts, two small attached eddies appear behind the stirrer. More vortices are shed as the stirrer moves along its path (see figure 4*a*). The rotation of these vortices is consistent with the stirrer's movement with CCW and CW vortices shed inside and outside

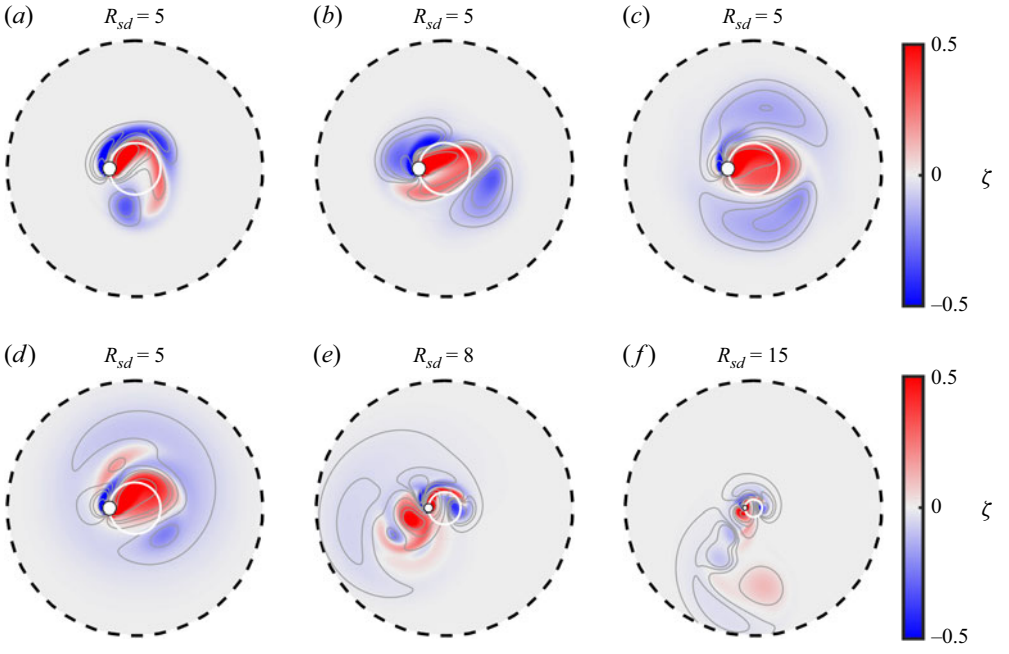

Figure 4. (*a–f*) Snapshots of the vorticity field in a Newtonian fluid, $Bn = 0$, $Re = 100$, at times $T = 1, 3, 10, 15, 30$ and 50. The white circle marks the stirrer's path, while grey lines represent the streamlines. The radius of the field of view is provided in the caption.

the stirrer's path, respectively. This is reminiscent of the archetypal problem of the flow around a cylinder of diameter $\hat{d}_s$ that moves at the constant velocity of $\hat{U}_o = \hat{r}_o\hat{\Omega}$. In the archetypal problem, laminar shedding in a Newtonian fluid of viscosity $\hat{\mu}$ and density $\hat{\rho}$ is expected at $40 \lesssim Re^* \lesssim 150$ where $Re^* = \hat{\rho}\hat{U}_o\hat{d}_s/\hat{\mu}$ (Roshko 1954).

Figure 4(*b*) represents the early dynamics following the onset of stirring. The periodic passage of the stirrer disrupts the formation and advection of CCW vortices, while CW vortices remain outside the stirrer's path, drifting slowly away (compare figures 4*b* and 4*c*). Meanwhile, as the attached eddies develop, the CCW eddy expands across the stirrer's path. When the stirrer moves through this eddy, it generates additional CCW vortices (see figure 4*d*). These CCW vortices also dissipate quickly before reaching beyond the central region.

Figure 4(*a*) also shows that the stirrer completes a period before the previously shed CW vortices advect away from the central region; e.g. during the second period ($1 \leqslant T \leqslant 2$), the stirrer interacts with the CW vortices shed during the first period. This mechanism interferes with vortex shedding: temporarily ($2 \leqslant T < 20$), the stirrer's path is surrounded by two CW vortices that interact with and follow the stirrer slowly moving away from the domain centre. The first two stages of mixing (stretching and folding of the interface followed by diffusion) take place concurrently with the vorticity dynamics discussed above.

At $T \approx 20$, the attached CCW eddy expands sufficiently to escape the stirrer's path (figure 4*e*). As this eddy gradually moves away from the central region, the approximate symmetry of the vorticity field, along with the corresponding symmetry in dye concentration in the central region (figure 3*e*), is disrupted. From this point onward, vortices are shed away from the central region, travelling far across the flow domain (figure 4*f*).

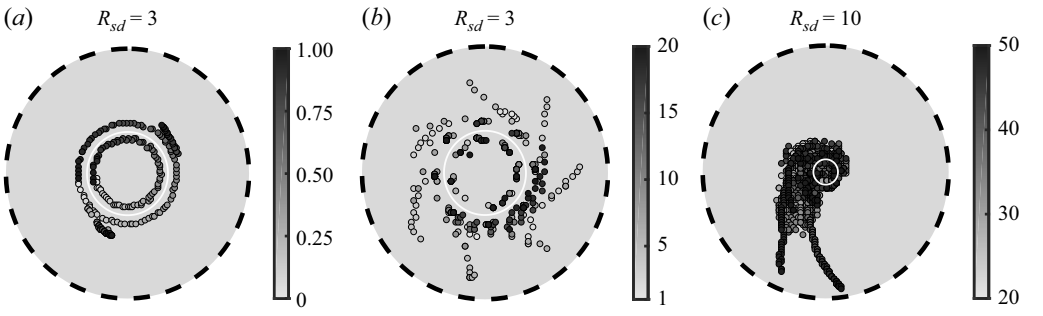

Figure 5. Time evolution of the vortex centres in a Newtonian fluid, $Bn = 0$, $Re = 100$, over different time intervals, as indicated by the colour bar. Lighter shades correspond to earlier times within each panel. The white solid line represents the stirrer's path, while the black dashed lines denote the subdomain boundary.

To better illustrate the stages of vortex development, we present an approximation of the locus of the vortex centres in figure 5. These centres, identified as the local minima and maxima of the vorticity field, correspond to the CCW and CW vortices, respectively. For simplicity and brevity, we refer to this collection of points as the vortex centres hereafter. When stirring begins, a pair of attached eddies forms and travels with the stirrer (figure 5*a*). Simultaneously, two CW vortices are shed outside the stirrer's path within the first period ($T \leqslant 1$). As shown in figure 5(*b*) , these shed vortices initially remain close to the central region, drifting away slowly. This quasi-periodic flow pattern leads to an approximately axisymmetric concentration field and a diffusion-dominated mixing phase. Finally, the vortices escape the central region, causing the well-mixed region to advect outward (figure 5*c*) – a stage marked by interface stretching and folding beyond the central region. The kinetic energy of escaping vortices decays exponentially due to viscous dissipation, allowing them to advect indefinitely. Consequently, mixing continues unbounded as the vortices transport dye farther into the flow domain.

Comparing the development of mixing and the vorticity field, we identify three key mechanisms promoting mixing during different stages of the flow: (i) local stretching and folding of the dye interface with the movement of the stirrer, (ii) diffusion-dominated mixing when flow structure is approximately steady and (iii) the advection of dye and stretching of the interface with vortices that escape the central region.

3.2. *Blending a viscoplastic fluid*

Figure 6 shows the development of the dye concentration when the fluid has a small yield stress, $Re = 100$ and $Bn = 0.025$. The dashed grey lines display the contours of $\tau = 1.01\,Bn$, a conservative estimate of the boundary of the yielded region. As before, the white and grey solid lines represent the stirrer's path and the streamlines, respectively.

The primary stages of mixing resemble those observed in the Newtonian case, beginning with the stretching and folding of the dye interface (figures 6*a* and 6*b*). This is followed by the formation of an approximately axisymmetric concentration profile and the emergence of a well-mixed region within the central area (figures 6*c* and 6*d*, respectively). As the well-mixed region drifts outward from the centre, the interface undergoes extensive stretching, accelerating the mixing process (figures 6*e* and 6*f*). A comparison between figures 3 and 6 further shows that the yield stress has little influence on the concentration field until the well-mixed region moves beyond the central area.

Figure 7 presents the evolution of the vorticity field at the same time instances as figure 6. Comparison with figure 4 illustrates that the vorticity fields are quite similar

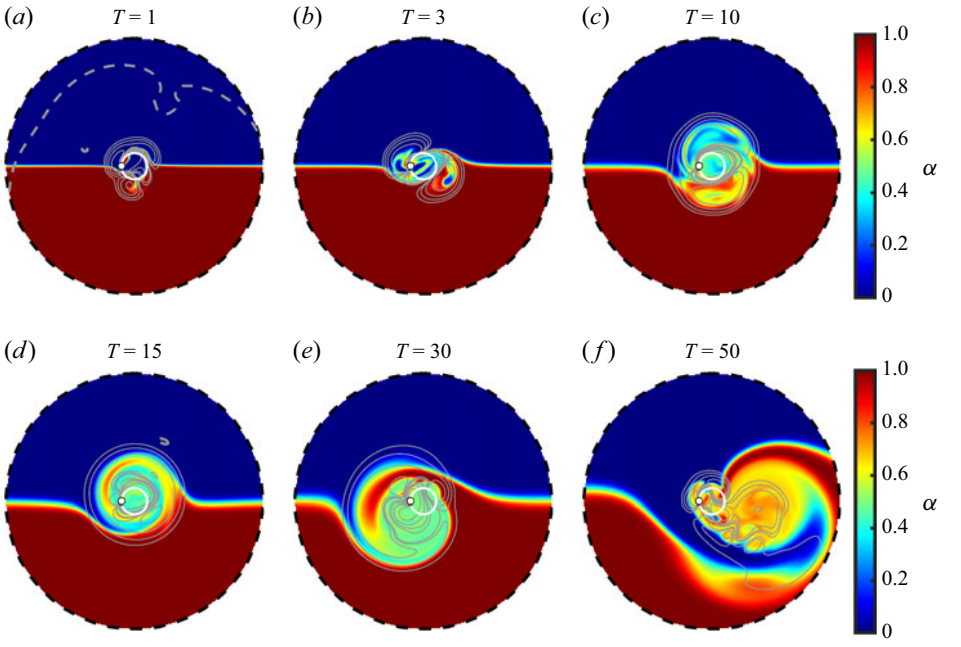

Figure 6. Snapshots of the dye concentration field in a VPF with a low yield stress, $Bn = 0.025$, $Re = 100$ and $R_{sd} = 10$. The white circle indicates the stirrer's path, grey lines represent streamlines and dashed grey lines show contours of $\tau = 1.01\,Bn$.

until vortices escape the central region. This indicates that, within the central region, the influence of the yield stress is negligible compared with purely viscous effects. However, outside this region, energy dissipation due to yield stress becomes increasingly significant with distance from the domain centre. Far enough from the centre, the fluid is expected to remain unyielded.

In the viscoplastic case, the escaped vortices predominantly drift in the azimuthal direction (see figures 7*e* and 7*f*). In contrast, in the Newtonian case, the radial displacement of the vortices is more pronounced. This highlights the first mechanism of mixing localisation in VPFs; when the fluid has a yield stress, escaped vortices are confined within a finite distance from the stirrer, effectively localising mixing. This behaviour contrasts with that of Newtonian fluids, where vortices can theoretically advect without bounds.

The effect of the yield stress on the vortex dynamics is further demonstrated in figure 8, which presents the time evolution of the approximate vortex centres over the same intervals as shown in figure 5. The similar development of vortices in the central region is evident in figures 8(*a*) and 8(*b*). However, a comparison of figures 5(*c*) and 8(*c*), reveals that the azimuthal movement of the vortex centres is more pronounced when $Bn > 0$.

Figure 9 illustrates the evolution of dye concentration at a moderate yield stress, $Bn = 0.4$. The approximate size of the yielded region is significantly smaller compared with the case of $Bn = 0.025$ (see dashed grey lines), and mixing remains relatively confined to the central region. The initial two stages of mixing are qualitatively similar to the previous cases: stretching and folding of the interface are followed by diffusion-dominated mixing, leading to the formation of a well-mixed region. However, in this case, the well-mixed region remains largely quiescent. The deformation of the dye interface does not extend beyond the central region.

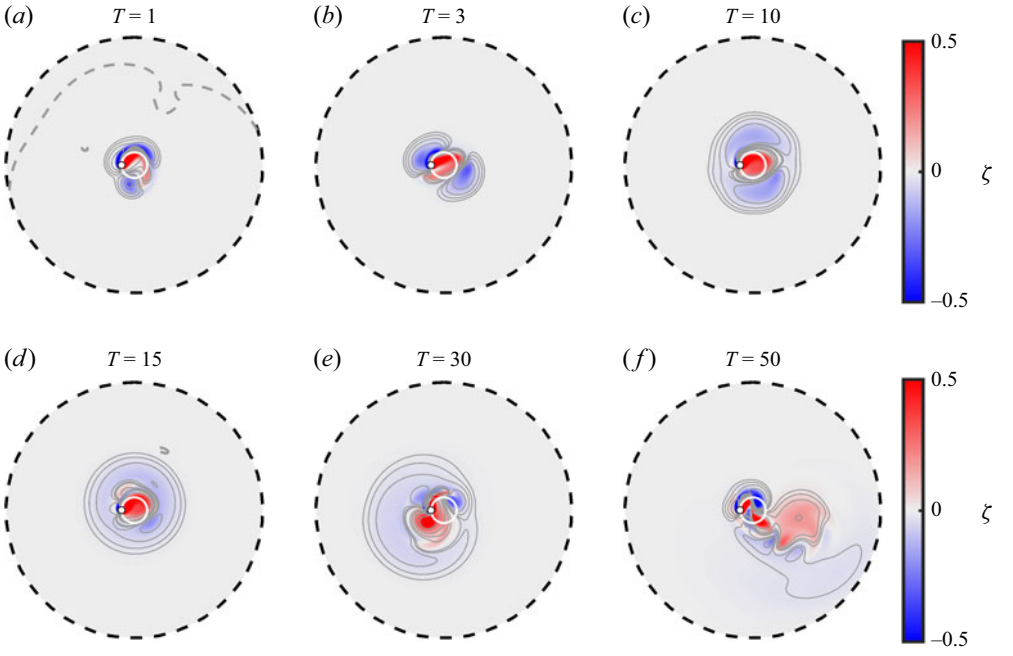

Figure 7. Snapshots of the vorticity field in a Newtonian fluid, a VPF with a low yield stress, $Bn = 0.025$, $Re = 100$ and $R_{sd} = 10$. The white circle indicates the stirrer's path, grey lines represent streamlines, and dashed grey lines show contours of $\tau = 1.01\,Bn$.

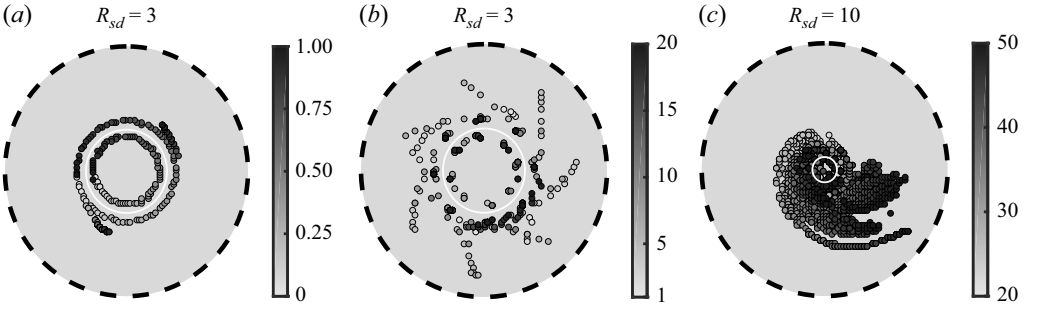

Figure 8. Time evolution of the vortex centres in a VPF with a low yield stress, $Bn = 0.025$, $Re = 100$, over different time intervals, as indicated by the colour bar. Lighter shades correspond to earlier times within each panel. The white solid line represents the stirrer's path, while the black dashed lines denote the subdomain boundary. The radius of the field of view is provided in the caption.

The evolution of the vorticity field at $Bn = 0.4$ is shown in figure 10. The initial shedding pattern appears similar to the Newtonian case (figure 10*a*). However, the shed CW vortices stay closer to the stirrer and the CCW eddy remains mostly confined within the stirrer's path because the yield stress suppresses the advection of shed vortices and growth of attached eddies. Consequently, the size of the well-mixed region is reduced compared with the previous cases. This localisation is closely connected to the development of vortices. Figure 11 illustrates the time evolution of the approximate vortex centres. The formation of the attached eddies and vortex shedding during the first period is similar to the previous cases (figure 11*a*). However, the shed vortices do not travel as far from the stirrer (figure 11*b*). Instead, they remain trapped in the vicinity of the stirrer's path (figure 11*c*).

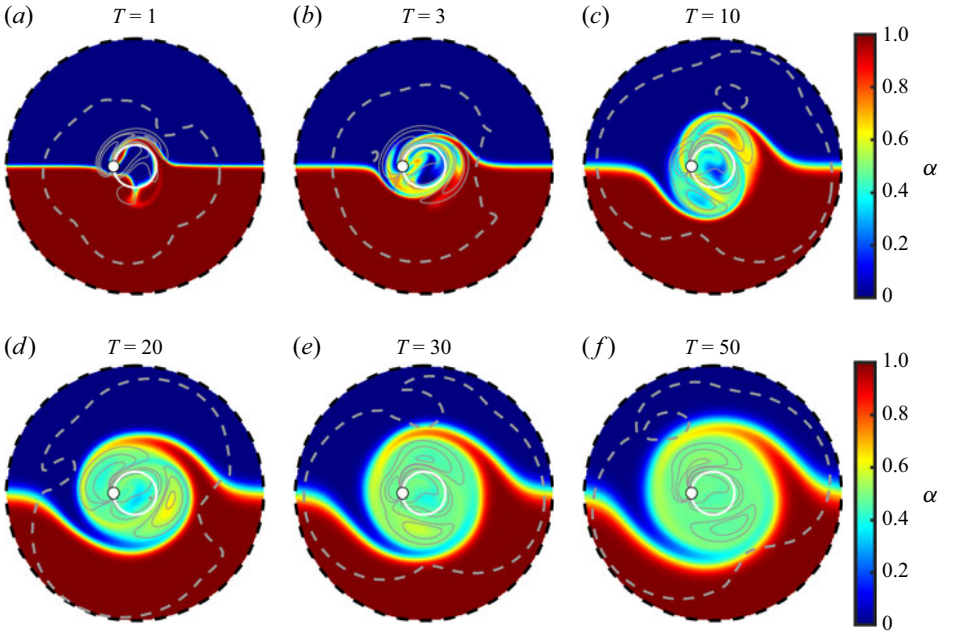

Figure 9. (*a–f*) Snapshots of the dye concentration field in a VPF with a moderate yield stress, $Bn = 0.4$, $Re = 100$ and $R_{sd} = 6$. The white circle indicates the stirrer's path, grey lines represent streamlines and dashed grey lines show contours of $\tau = 1.01\,Bn$.

As a result, mixing remains confined to the central area throughout the process (figure 9*f*). This behaviour represents the second mechanism of mixing localisation due to yield stress; as shed vortices remain trapped near the stirrer, the stretching and folding of the interface are confined to this region, limiting the mixing rate.

As expected, at higher-yield-stress values, mixing becomes increasingly confined to the central region. An illustrative case for $Bn = 1$ is shown in figure 12, where the first and second rows display the evolution of dye concentration and vorticity fields, respectively. The dye concentration rapidly assumes an approximately axisymmetric distribution, after which mixing is primarily governed by radial diffusion. The two eddies remain attached to the stirrer, with no vortex shedding observed. This behaviour is further illustrated in figure 13, showing the time evolution of the approximate vortex centres. This represents the third mode of localisation; the complete suppression of vortex shedding, where interface deformation remains largely confined to the central region.

Increasing Bn beyond $Bn \sim 1$ does not introduce significant qualitative changes to the mixing dynamics. Figure 14 presents a representative case at $Bn = 100$ ($Bn \gg 1$), where the evolution of concentration and vorticity fields are shown in the first and second rows, respectively. Compared with $Bn = 1$ (see figures 12*a* and 14*a*), interface deformation after the first stirring period is markedly reduced. The stirrer fails to draw the interface deep into the dye-free region because the yielded zone is much smaller than in the $Bn = 1$ case. Indeed, the stirrer's trajectory now partially traverses unyielded regions. The yielded zone quickly settles into a steady configuration relative to the stirrer. Both the size and shape of the yielded region resemble the asymptotic case of a cylinder translating through a VPF in the high-yield-stress limit (Tokpavi, Magnin & Jay 2008; Supekar, Hewitt & Balmforth 2020). Initially, the interface within this region is periodically stretched by successive passages of the stirrer (figures 14*a* and 14*b*). However, mixing soon becomes diffusion

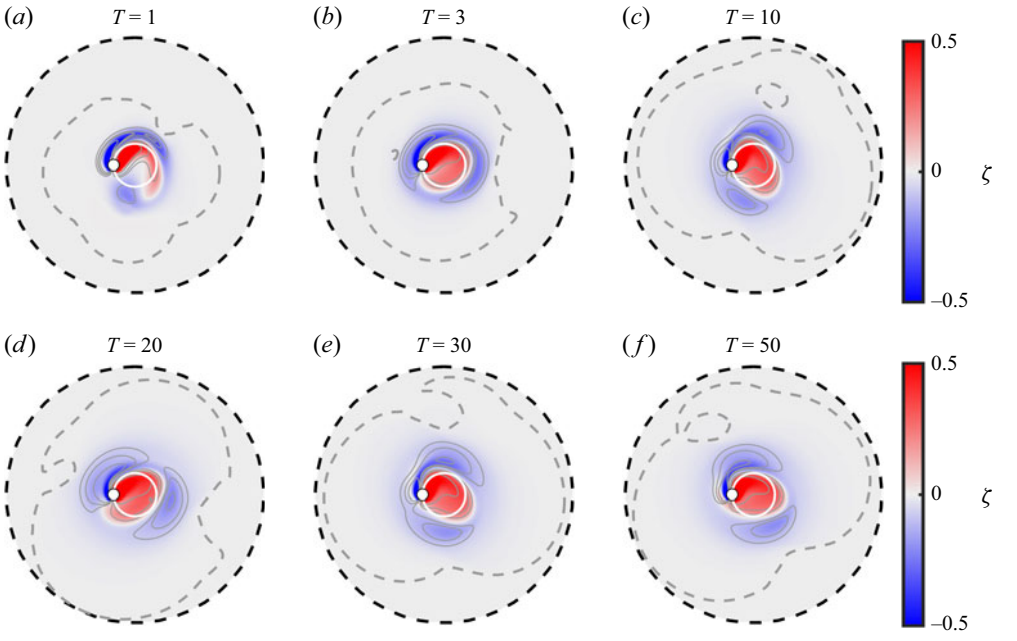

Figure 10. (*a–f*) Snapshots of the vorticity field in a VPF with moderate yield-stress value, $Bn = 0.4$, $Re = 100$, $R_{sd} = 6$. The white circle indicates the stirrer's path, while the grey lines depict the streamlines. The dashed grey lines display the contours of $\tau = 1.01\,Bn$.

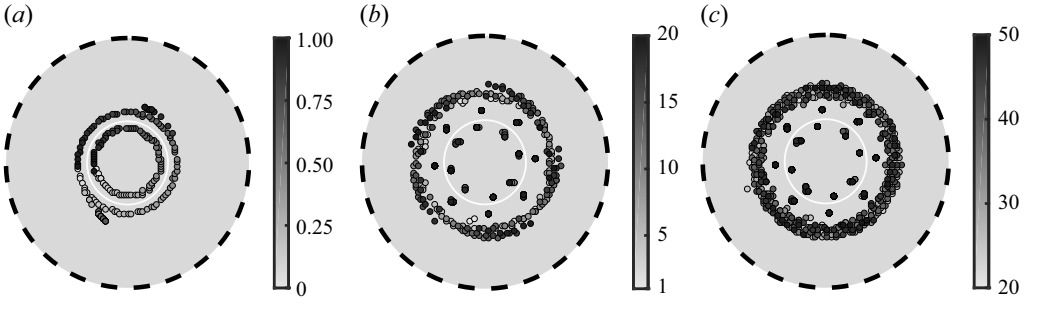

Figure 11. The time evolution of the vortex centres in the VPF with a moderate yield stress, $Bn = 0.4$, $Re = 100$ and $R_{sd} = 3$, over different time intervals, as indicated by the colour bar. Lighter shades correspond to earlier times within each panel. The white solid line represents the stirrer's path, while the black dashed lines denote the subdomain boundary.

dominated as a well-mixed core develops (figures 14*c* and 14*d*). Figure 14(*e–h*) highlights the rapid establishment of a flow field that is steady in the stirrer's frame and strongly localised around it. Instead of extending along the stirrer's trajectory, the attached eddies stretch predominantly in the radial direction, which explains the limited elongation of the interface along the path of the stirrer.

To compare mixing rates across different regimes, we present the normalised variance of dye concentration, σ^2_{15}, in figure 15. For reference, the solid blue line shows the purely diffusive case. As expected, mixing rates decrease with increasing Bn. At low Bn (e.g. $Bn = 0.05$), initially the mixing curves closely match the Newtonian case, indicating that, at low yield stress, while the flow remains confined to the central region ($T \lesssim 10$), yield stress has a negligible effect on local energy dissipation. However, the influence of yield

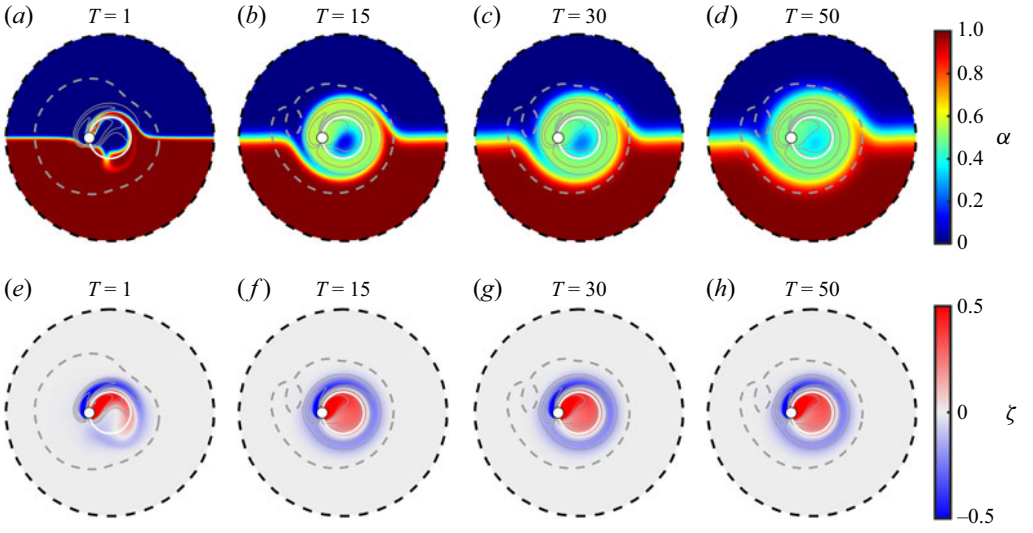

Figure 12. Snapshots of the dye concentration (*a–d*) and vorticity (*e–h*) fields in a VPF with a high yield stress, $Bn = 1$, $Re = 100$ and $R_{sd} = 5$. The white circle indicates the stirrer's path, grey lines represent streamlines and dashed grey lines show contours of $\tau = 1.01\,Bn$.

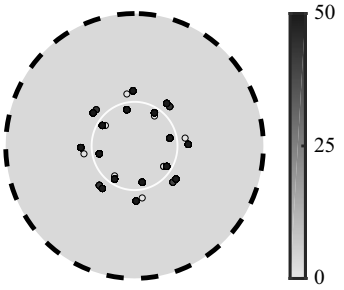

Figure 13. The time evolution of the vortex centres in the VPF with a high yield stress, $Bn = 1$, $Re = 100$ and $R_{sd} = 3$. Lighter shades correspond to earlier times. The white solid line represents the stirrer's path, while the black dashed line denotes the subdomain boundary.

stress becomes more pronounced in later stages, as the well-mixed region drifts outward (see $T \approx 20$ and $T \approx 30$ for $Bn = 0.025$ and $Bn = 0.05$, respectively). This shift occurs when the dye interface enters a region where the energy dissipation and flow dynamics begin to be affected by the yield stress. From this stage onward, the σ_{15}^2 curves diverge, as the advection of escaped vortices is increasingly suppressed by the yield stress.

At moderate Bn, the divergence of σ_{15}^2 from the Newtonian case becomes apparent earlier. This is because, as Bn increases, the dissipation caused by yield stress starts to influence smaller radii. The downward concavity in the variance is almost entirely suppressed, as vortices remain confined within the central region, preventing them from re-accelerating mixing.

The mixing rate decreases progressively with increasing Bn, reflecting both the overall slowdown of the flow and the suppression of vortices. For $Bn \gtrsim 1$, however, it shows little further variation. To assess these changes, we measure the mixing rate during the final, diffusion-dominated stage, where the concentration variance follows an exponential decay

$$\sigma_{15}^2 \approx \sigma_0^2 \exp\left(-2\lambda T\right). \tag{3.2}$$

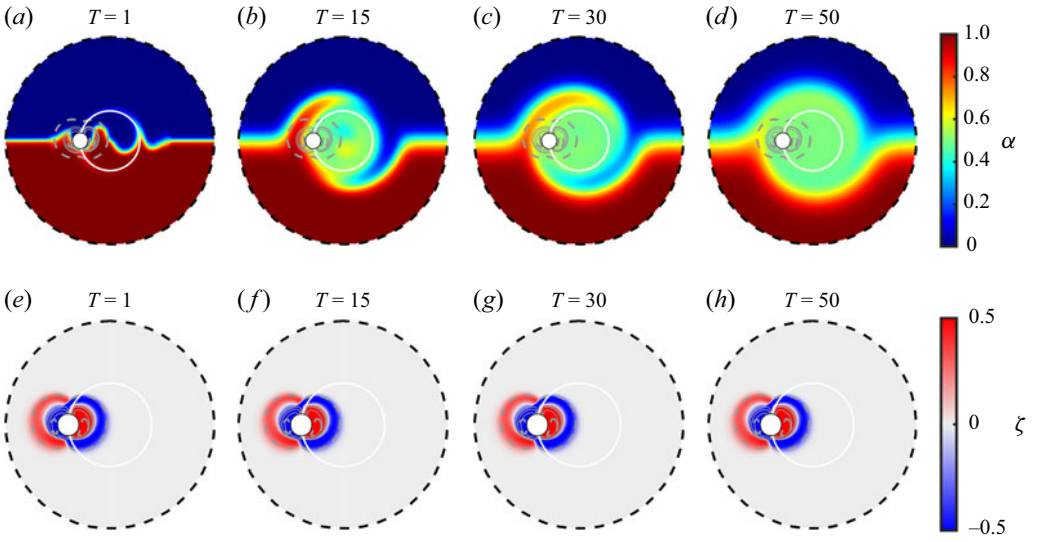

Figure 14. Snapshots of the dye concentration (*a–d*) with $R_{sd} = 3$ and vorticity field (*e–h*) with $R_{sd} = 2$, in a VPF with a high yield stress, $Bn = 100$ and $Re = 100$. The white circle indicates the stirrer's path, grey lines represent streamlines and dashed grey lines show contours of $\tau = 1.01\,Bn$.

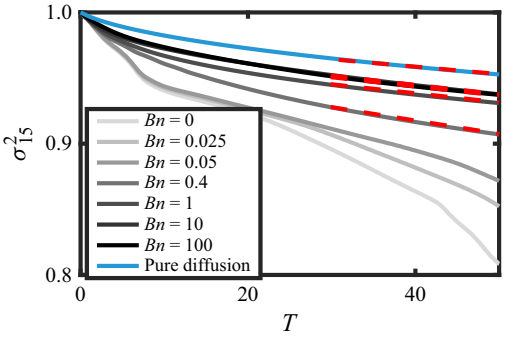

Figure 15. Evolution of the normalised dye concentration variance for $0 \leqslant Bn \leqslant 100$. Darker shades of grey correspond to higher Bn values; the curves for $Bn = 10$ and $Bn = 100$ nearly overlap and are not visually distinguishable. The solid blue line denotes pure diffusion, and the red dashed lines show exponential fits during the diffusion-dominated stage. $Re = 100$.

Here, λ is the decay constant. The red dashed lines in figure 15 depict the exponential fits. Following Christov & Homsy (2009), we define the enhancement factor $\eta_\lambda = \lambda/\lambda_p$, where λ_p is the decay constant for the purely diffusive case. The intercept of the exponential fit, σ_0, can be viewed as an approximation of the standard deviation when the diffusion-dominated phase begins, providing a measure of mixing by the end of the advection-dominated stage. Here, a second enhancement factor is defined as $\eta_\sigma = \sigma_{op}/\sigma_0$, where σ_{op} is the intercept of the exponential fit for the purely diffusive case. This enhancement factor, η_σ, enables comparison of the extent to which mixing is achieved during the initial phase dominated by interface stretching.

The variation of enhancement factors with Bn is shown in figure 16. Changes in η_λ are more pronounced than those in η_σ. This suggests that the long-term impact of yield stress on mixing can be more significant than its short-term effects; increasing the Bingham number by approximately three orders of magnitude reduces η_σ by approximately 10 %,

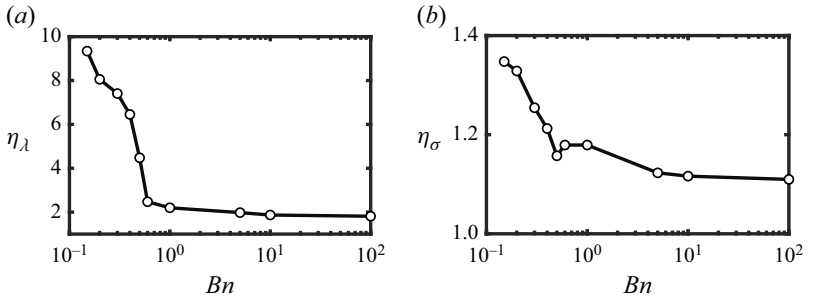

Figure 16. Variation of the enhancement factors (*a*) η_λ and (*b*) η_σ with Bn at $Re = 100$.

attributed to the suppression of dye interface stretching during the initial mixing stage. Meanwhile, the same increase in Bn results in an approximately 80 % reduction in η_λ, as diffusion – the dominant mixing mechanism over longer time scales – becomes less effective when the interface area is reduced. Lastly, both enhancement factors drop relatively sharply for small Bn, but exhibit only a slow decline beyond $Bn \sim 1$. This behaviour is discussed in greater detail in § 3.3.

3.3. *Flow and mixing regimes*

In the previous section, we identified three distinct mixing regimes:

Regime SE (shedding, escaped vortices): at sufficiently low Bn, mixing is initially dominated by the stretching and folding of the interface. This is followed by a brief period where mixing is driven primarily by radial diffusion. In this regime, vortices escape the central region, carrying dye and stretching the interface deep into the domain. Once the vortices escape, mixing re-accelerates, driven by advection and further interface stretching.

Regime ST (shedding, trapped vorticed): at moderate Bn, mixing does not re-accelerate after the diffusion-dominated phase. In this regime, the shed vortices remain trapped in the central region, unable to escape. They are periodically influenced by the passage of the stirrer but remain confined, limiting further advection-driven mixing.

Regime NS (no shedding): at sufficiently high Bn, mixing is quickly dominated by diffusion. The yield stress completely suppresses vortex shedding, confining interface stretching to the immediate vicinity of the stirrer.

The mixing regimes described above are closely tied to the flow development and vortex dynamics. To facilitate comparison and distinction of the regimes, we examine the time evolution of kinetic energy (approximated by the velocity norm, $||u||$) and the size of the moving region. For the latter, we consider the general condition illustrated in figure 17. Here, r_{yo} and r_{yi} mark the farthest and closest points where the line connecting the domain centre to the stirrer-path centre crosses the boundary of the quiescent unyielded region.

When the fluid is Newtonian ($Bn = 0$), $r_{yi} = 0$ and $r_{yo} \to \infty$. On the other hand, if the fluid has a yield stress ($Bn > 0$), then $r_{yo} < \infty$. Furthermore, the results presented above (e.g. $Bn = 0.4$ shown in figure 9) illustrate that, at sufficiently small Bn, $r_{yi} = 0$. Nevertheless, at sufficiently large Bn (see, e.g. $Bn = 100$ shown in figure 14), $r_{yi} > 0$.

Figure 18(*a*) shows the time evolution of r_{yo} at $Re = 100$. In regimes SE and ST, r_{yo} evolves on two distinct time scales: a shorter time scale ($T_s \approx O(1)$), corresponding to small oscillations in r_{yo}, and a much longer time scale ($T_l \approx O(10)$), associated with the overall increase in r_{yo}. The amplitude of the oscillations diminishes as Bn increases, eventually disappearing entirely in regime NS. The white dashed lines in figure 18(*a*)

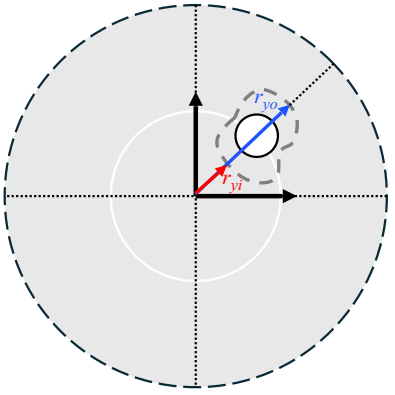

Figure 17. Schematic of the moving-region boundary (dashed grey line), with r_{yi} (red) and r_{yo} (blue) marking the nearest and farthest intersections of the line from the domain centre to the stirrer-path centre with the boundary of the quiescent unyielded region.

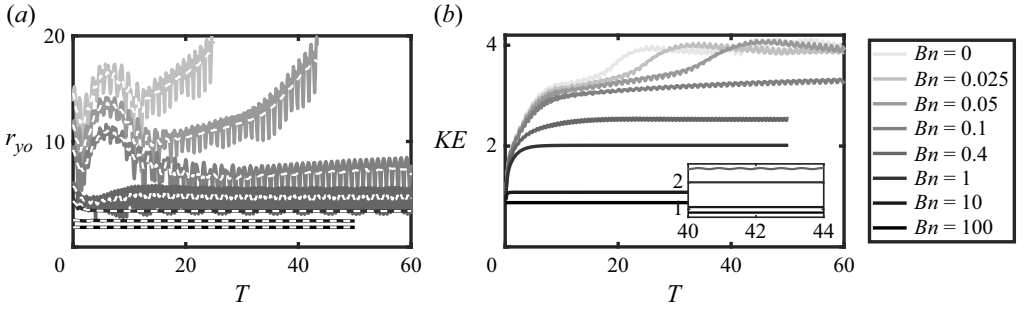

Figure 18. (*a*) Time evolution of the outer radius of the yielded region, r_{yo}, at different yield-stress values. Darker grey shades correspond to larger Bn. The white dashed lines display the moving time average ($\overline{r}_{yo}$). (*b*) Time evolution of the velocity norm at different yield-stress values. The inset provides a magnified view over the range $40 < T < 44$ for regimes ST and NS. $Re = 100$.

display the moving time average ($\overline{r}_{yo}$) with an averaging window of $T = 1$, which better illustrates variations over longer time scales.

Immediately after stirring begins, r_{yo} rises sharply, reflecting the onset of yielding. The oscillations in r_{yo} observed in regimes SE and ST (e.g. $Bn = 0.025$ and $Bn = 0.4$) are linked to vortex interactions, indicating that the moving region remains unsteady relative to the stirrer. By contrast, in regime NS, vortex shedding and escape from the central region do not occur; instead, r_{yo} rapidly converges to a steady value, suggesting that the flow is steady in the stirrer's frame of reference. This steady value depends only weakly on Bn: increasing Bn by two orders of magnitude reduces r_{yo} by less than 50 %.

At very large Bn, the flow configuration and moving region resemble the asymptotic case of a cylinder translating through a VPF in the high-yield-stress limit. For instance, at $Bn = 100$ the moving region corresponds to $r_{yo} \approx 1.86$, only slightly larger than the plastic limit of $r_{yo} \approx 1.70$ for uniform flow past a cylinder (Supekar *et al.* 2020). This explains the very slow decrease of the mixing rate at $Bn \gtrsim 1$ (see figure 16); in regime NS, the moving region very slowly approaches the plastic limit with $\lim_{Bn\to\infty} r_{yo} \sim 1.70$. At high Bn, the radial extent of interface deformation is thus restricted, while stretching along the stirrer's

path diminishes with increasing Bn. We hypothesise that these two effects together account for the very slow decay of mixing efficiency when $Bn \gtrsim 1$ (see figure 16).

In regime SE, r_{yo} increases to a local maximum as the CW shed vortices travel away from the stirrer, orbiting the stirrer's path (see $T \approx 5$ and $Bn = 0.025$ in the figure). r_{yo} decreases as these satellite vortices spread azimuthally and weaken. The final increase in r_{yo} corresponds to the escape of vortices from the central region (e.g. $T \approx 20$ for $Bn = 0.025$). Although we expect r_{yo} to approach an upper bound for $Bn \geqslant 0$, numerical estimation of this ultimate threshold in regime SE was not feasible within the computational domain used in this study. However, the approach of r_{yo} to a steady average value, $\bar{r}_{ys}$, is clear in regimes ST and NS (see red dashed lines in the figure).

Finally, in regime ST, the relatively slow increase in r_{yo} during the early stages (see $Bn = 0.4$, $T \lesssim 10$) confirms that the yield stress delays the advection of shed vortices away from the stirrer. Additionally, no further increases in r_{yo} are observed, as the vortices remain confined within the central region.

Figure 18(*b*) shows the time evolution of the kinetic energy. As with r_{yo}, the kinetic energy exhibits two characteristic time scales: a short time scale ($T_s \approx O(1)$), corresponding to small oscillations in KE, and a longer time scale ($T_l \approx O(10)$), reflecting the overall growth of KE. The oscillation amplitude again diminishes with increasing Bn, disappearing entirely in regime NS. Here, KE increases rapidly when stirring begins, before reaching an apparently quasi-steady state (see, e.g. $Bn = 0.05$, $10 \lesssim T \lesssim 25$). This corresponds to the time interval when the shed CW vortices advect within the central region. In regime SE, this stage is followed by a second, relatively rapid increase, corresponding to the escape of vortices from the central region (see, e.g. $Bn = 0.05$, $30 \lesssim T \lesssim 45$). This transition is not observed in regime ST, where shed vortices remain trapped in the central region (see, e.g. $Bn = 0.4$ in the figure).

Two critical values of Bn may be identified to distinguish the three regimes.

$$\begin{cases} \text{Regime SE} & \text{if} \quad Bn \leqslant Bn_{ce}, \\ \text{Regime ST} & \text{if} \quad Bn_{ce} \leqslant Bn \leqslant Bn_{ct}, \\ \text{Regime NS} & \text{if} \quad Bn_{ct} \leqslant Bn, \end{cases} \tag{3.3}$$

where Bn_{ce} and Bn_{ct} are the critical Bingham numbers marking the regime transitions.

To differentiate the regimes, we evaluated the Fourier spectrum of the oscillations, $KE' = KE - \overline{KE}$, where $\overline{KE} = \int_T^{T+1} KE \, \mathrm{d}T$. Figure 19 shows the frequency spectrum of KE' at $Re = 100$, $0 \leqslant Bn \leqslant 100$. All regimes have peaks at frequency one and its harmonics. This is the fundamental frequency of the system for all Bn considered. The prominence of the peaks diminishes as Bn increases. Regimes SE and ST have additional distinct peaks (see $f \approx 1.6$ and 1.8, respectively, in figure 19). These characteristic peaks vanish as mixing transitions between regimes. In contrast, regime NS does not display any peaks beyond the fundamental frequency and the harmonics. To estimate the critical values, we evaluated the strength of the characteristic peak for each regime and used the two closest data points to find, by extrapolation, the Bn value at which the characteristic peak disappears.

Figure 20 illustrates the flow regime map in the (Re, Bn) plane. The orange, green and blue zones correspond to regimes NS, ST and SE, respectively. Regimes SE and ST disappear at sufficiently small Re below which there is no shedding even in the Newtonian case. The square and circle markers indicate the estimates of Bn_ce and Bn_{ct}, respectively.

The dashed and dotted lines in figure 20 illustrate that the variations of Bn_{ct} and Bn_ce are well described by the following fits:

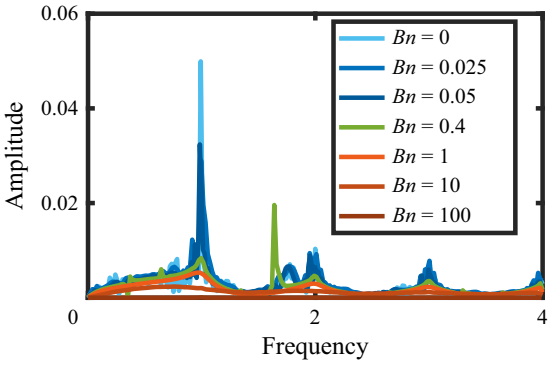

Figure 19. Fourier spectrum of KE'. Here, $Re = 100$.

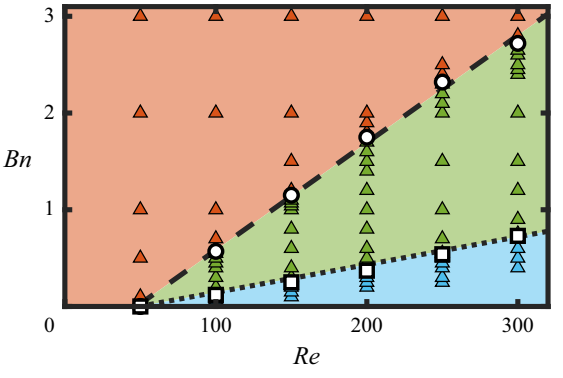

Figure 20. Flow regime map in the (Re, Bn) plane. Regimes NS, ST and SE, are indicated in orange, green and blue, respectively. The triangle markers are the data points. Square and circle markers display the estimates of Bn_{ce} and Bn_{ct}, respectively. The black dotted and dashed lines are linear fits to Bn_{ce} and Bn_{ct}.

$$\begin{aligned} Bn_{ce} &= 0.00287Re - 0.14, \\ Bn_{ct} &= 0.0111Re - 0.53. \end{aligned} \tag{3.4}$$

The linear variation of the critical Bingham numbers with Re is reminiscent of the effective Reynolds number, Re_e, in flows of VPFs

$$Re_e = \frac{\hat{\rho}\hat{U}_o^2}{\hat{\tau}_y + \hat{\mu}\hat{\dot{\gamma}}_c}, \tag{3.5}$$

where $\hat{\dot{\gamma}}_c$ is the characteristic strain rate. The primary challenges in identifying the characteristic strain rate in flows of VPFs are twofold: firstly, the physically representative $\hat{\dot{\gamma}}_c$ may vanish as yield stress increases and the fluid becomes quiescent. Secondly, the relationship between $\hat{\dot{\gamma}}_c$ and yield stress is not known *a priori*; see Thompson & Soares (2016) and Ahmadi, Olleik & Karimfazli (2022) for more details.

In this context, the linear critical equations presented in (3.4) reveal the effective Reynolds numbers at which regime transitions occur. Assume that $\hat{U}_o = \hat{r}_o\hat{\Omega}$ and $\hat{\dot{\gamma}}_c = a\hat{\Omega}$, where a is a constant, then (3.5) yields

$$Re_e = \frac{Re}{a + Bn}. \tag{3.6}$$

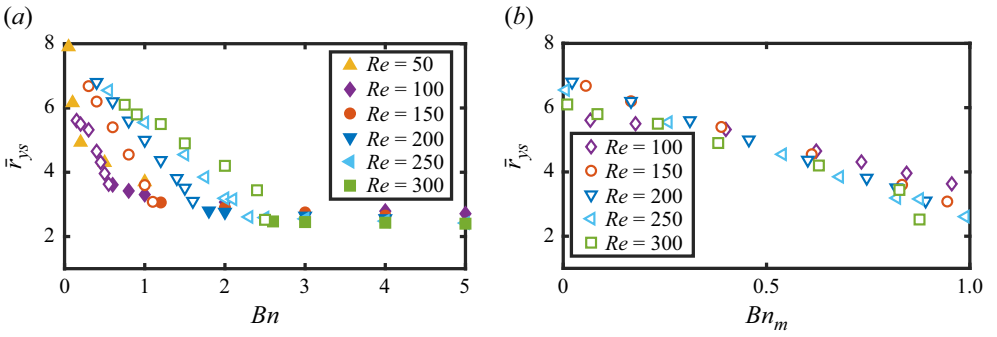

Figure 21. (*a*) Steady values of the time-averaged radius of the yielded region, $\bar{r}_{ys}$, at different Bn and Re. Each symbol (with unique colour) corresponds to a specific Re; empty and filled symbols denote regimes ST and NS, respectively. (*b*) Evolution of $\bar{r}_{ys}$ in regime ST as a function of the modified Bingham number, $Bn_m = (Bn - Bn_{ct})/(Bn_{ce} - Bn_{ct})$.

Comparing this with (3.4), we find

$$\begin{aligned} Re_{e,ce} &= \frac{Re}{Bn_{ct} + 0.53} \approx 350, \quad a_{ce} \approx 0.14, \\ Re_{e,ct} &= \frac{Re}{Bn_{ce} + 0.14} \approx 90, \quad a_{ct} \approx 0.53. \end{aligned} \tag{3.7}$$

In the limit corresponding to Newtonian fluids ($Bn \to 0$), the effective Reynolds number is given by $Re_e = Re/a$. On the other hand, as $c \to \infty$, the critical Reynolds number beyond which the wake behind a cylinder in a free stream of Newtonian fluids becomes unstable is (Roshko 1954)

$$Re^*_{cr} = \frac{Re_{cr}}{c} \approx 40, \tag{3.8}$$

which implies that, for $c \to \infty$, $Re_{cr} \approx 80$, or alternatively $Re_{e,ct} \approx Re_{cr}/a_{ct} \approx 151$, marks the onset of wake instability. Comparing these values with $Re_{e,ct}$ when $c = 2$ (see 3.7) suggests that the wake behind the cylinder becomes more unstable as the path curvature decreases.

The two distinct definitions of the effective Reynolds number shown in (3.7) confirm that, for a given flow set-up, the characteristic strain rate changes with Bn. It follows that defining a unique effective Reynolds number that fully describes the hydrodynamics observed in the (Re, Bn) plane, e.g. help distinguish the different regimes at different values of the Bingham number, is not feasible.

To quantitatively compare the extent of localisation in different regimes, figure 21(*a*) displays the steady time-averaged radius of the moving region, $\bar{r}_{ys}$, in regimes ST and NS for a wide range of Re. Distinct colours and marker shapes represent various Re values. Empty and filled markers indicate regimes ST and NS, respectively.

In regime ST, $\bar{r}_{ys}$ decreases with decreasing Re and increasing Bn, confirming the influence of both yield stress and purely plastic stresses on the flow field. Figure 21(*b*) shows that, in this regime, $\bar{r}_{ys}$ values approximately collapse onto the same curve when plotted against a scaled Bingham number, Bn_m,

$$Bn_m = \frac{Bn - Bn_{ct}}{Bn_{ce} - Bn_{ct}}. \tag{3.9}$$

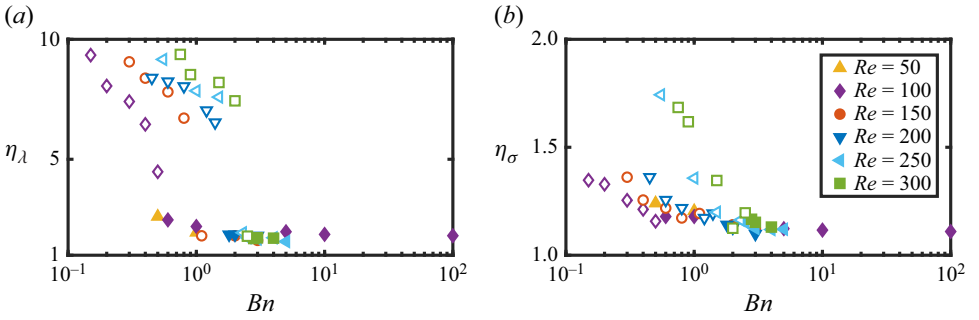

Figure 22. Variation of enhancement factors, (*a*) η_λ and (*b*) η_σ with *Bn* and *Re*. Each symbol with unique colour shows a specific *Re*. The empty and filled symbols indicate regimes ST and NS, respectively.

Additionally, figure 21(*a*) reveals that $\bar{r}_{ys}$ is approximately independent of *Re* in regime NS. Furthermore, in line with the limited changes in the mixing rate at high Bingham ($Bn \gtrsim 1$), $\bar{r}_{yo}$ changes very slowly with *Bn* within this range.

Finally, figure 22 illustrates the variation of enhancement factors with *Bn* across different *Re*. Different values of *Re* are distinguished by different marker shapes. Empty and filled symbols indicate regimes ST and NS, respectively. The initial rapid decrease in η_λ and η_σ, similar to the trend observed in figure 16, corresponds to regime ST. The enhancement factors show little variation in regime NS. This suggests that the suppression of advected shed vortices plays a significantly larger role in mixing localisation and reduction than the contraction of the sheared layer around the stirrer, the sole localisation mechanism active in regime NS. Moreover, the sharpest decline occurs near the transition to regime NS, indicating that the complete suppression of shedding marks a key threshold in the localisation process.

It is also evident that the influence of a small yield-stress value is more pronounced at lower *Re*; for instance, comparing $Re = 100$ and $Re = 300$ in the figure. At higher *Re*, the influence of *Bn* on the enhancement factors is less pronounced at low *Bn*, and a very sharp decline in the enhancement factors is observed near $Bn \lesssim Bn_{ct}$.

4. Summary

In this study, we investigated a canonical two-dimensional mixing set-up to establish a mechanistic understanding of how fluid mechanics drives transitions in the mixing regimes of yield-stress fluids.

Our numerical simulations model an infinite, two-dimensional domain filled with a quiescent VPF described by the Bingham model. In this set-up, a cylinder moves at a constant speed along a circular path, stirring a fluid with uniform density and rheological properties. The stirrer diameter is fixed at half the stirring radius throughout the study. The bottom half of the domain is initially marked with a passive dye, with the centre of the stirrer's path aligned with the dye interface. This representative model allowed us to explore the fundamental features of yield-stress fluid mixing in two-dimensional settings.

To decouple the influence of the flow dynamics from dye concentration, we considered only one-way coupling, where the flow is unaffected by dye concentration changes. This approach simplifies the isolation of causal relationships between fluid mechanics phenomena and mixing events.

In the Newtonian case, we identified three primary mixing mechanisms when stirring a fluid with heterogeneous dye distribution: (i) the stretching and folding of the dye interface

within the central region as the stirrer initiates movement, (ii) diffusion-dominated mixing when dye distribution becomes approximately uniform along streamlines and (iii) enhanced mixing due to vortex shedding, where shed vortices transport dyed regions into dye-free areas (or *vice versa*), significantly extending the dye interface.

For the laminar regimes studied, the fluid dynamics evolves on two time scales: the average energy of the system changes on a slow time scale, roughly an order of magnitude slower than the stirrer period, while energy oscillations, related to vortex interactions, occur on a faster time scale. As yield stress increases, the average yielded region size, kinetic energy and energy oscillations decrease, eventually leading to oscillation suppression. We identified three mechanisms by which yield stress localises mixing.

(i) Finite vortex advection: in yield-stress fluids, advection of shed vortices is suppressed, with vortices travelling within a finite radius from the stirrer due to energy decay. This defines a maximum distance for dye transport and leads to localised mixing.
(ii) Entrapment of shed vortices: at moderate yield stresses, shed vortices cannot escape the stirrer's vicinity, resulting in periodic interactions between the stirrer and previously shed vortices, which promote mixing localisation.
(iii) Suppression of vortex shedding: at high yield stresses, vortex shedding ceases entirely, confining mixing to the interface stretching caused by direct interaction between the stirrer and the dye interface.

We classified the observed mixing regimes based on these mechanisms: in regime SE, shed vortices escape the central region, causing dye variance evolution similar to that in Newtonian fluids, with mixing initiated by interface stretching and folding, followed by a diffusion-dominated phase and then acceleration by escaping eddies. Regime ST is defined by the entrapment of vortices near the stirrer, limiting mixing to its immediate vicinity, while regime NS shows no vortex shedding, with mixing characterised by initial interface stretching followed by diffusion across streamlines and across the boundaries of the well-mixed region.

Using a fast Fourier transform on energy oscillations, we distinguished these regimes, all featuring a fundamental mode at frequency one. Additional spectral peaks in regimes SE and ST, introduced by shed vortices, further enabled us to identify critical transition criteria. In the (Re, Bn) plane, we observed distinct separation of the three regimes along lines that relate critical Bingham numbers to Reynolds numbers. This relationship allows us to define two unique, effective Reynolds numbers, each capturing a transition between two regimes at a constant value. This supports the hypothesis that fluid mechanics phenomena underlying mixing regime transitions are closely linked to the bluff-body flow dynamics, traditionally described by threshold Reynolds numbers marking stability and flow transition modes.

Comparing the decay of dye concentration variance, σ^2, across regimes, we hypothesise that, among the various localisation mechanisms, vortex entrapment near the stirrer has the most significant impact on mixing. This is supported by the contrasting long-term decay behaviours observed in regimes SE and ST: in regime ST, where vortices remain entrapped, σ^2 shows an exponential decay, while in regime SE, it decays at an accelerating rate due to the influence of vortices that escape into the outer regions. To compare regimes ST and NS, we introduced an enhancement factor, η_λ, which quantifies the relative decay rate of σ^2 during the final, diffusion-dominated stage of mixing, compared with the purely diffusive case. In regime ST, η_λ declines sharply with increasing Bn, but in regime NS, it becomes largely independent of both Re and Bn. This suggests that vortex entrapment is indeed the

primary driver of mixing localisation. Moreover, once vortex shedding is fully suppressed (in regime NS), increasing stirrer speed has minimal effect on enhancing mixing.

Finally, mixing localisation has far-reaching effects beyond the initial localisation of interface stretching: while the change in the degree of mixing by the end of the advection-dominated phase may not be very significant (e.g. approximately 10 % for an increase of three orders of magnitude in Bn), the subsequent change in the decay rate of σ^2 can be much more significant (more than 80 %).

The fundamental principle of laminar mixing in stirred tanks is the periodic movement of a stirrer along a closed path. In this work, we model this process in its most simplified form: a single stirrer moving along a circular path across an initial concentration gradient, within an effectively infinite domain. The dynamics is governed by Re and Bn and c. For a fixed stirring radius, we observe a gradual transition from attached eddies to vortex shedding, with vortices either remaining trapped around the stirrer or escaping the central region.

The vortex dynamics identified in this study is closely linked to the classical problem of vortex shedding behind bluff bodies. The Strouhal number associated with vortex shedding behind bluff bodies, defined as $St = \hat{f}\hat{d}_s/(\hat{r}_o\hat{\Omega})$, increases monotonically with Re and asymptotically approaches a maximum value, St_m. Here, $\hat{f}$ is the shedding frequency. In contrast, St is expected to decrease with increasing Bn, as the effective Reynolds number is reduced. Accordingly, variations in c are expected to produce more complex vortex structures, since the maximum number of vortices shed per stirrer period scales with cSt_m. A detailed investigation of the influence of c lies beyond the scope of the present study. Nevertheless, we hypothesise that, in the absence of wall effects, the primary mixing modes and yield-stress-driven localisation mechanisms identified here remain relevant. Qualitatively, the archetypal regimes fall into three categories: NS (no shedding), ST (shedding with trapped vortices), and SE (shedding with escaping vortices).

For passive tracers, the transitions between the mixing regime observed here correlate with distinct effective Reynolds numbers based on the stirrer size, shape and speed, alongside the Bingham number. Alternatively, the critical Bingham numbers marking these transitions are expected to scale linearly with the Reynolds number based on purely viscous stresses. Given the lack of an *a priori* definition for effective Reynolds numbers in such flows, we recommend further investigation of the linear critical criteria observed here.

Funding. We gratefully acknowledge financial support from Natural Sciences and Engineering Research Council (NSERC), Canada, through the Discovery Grant program. This research was enabled in part by support provided by Calcul Québec (www.calculquebec.ca) and Compute Canada (www.computecanada.ca).

Declaration of interests. The authors report no conflict of interest.

References

Ahmadi, A., Olleik, H. & Karimfazli, I. 2021 A quantitative evaluation of viscosity regularization in predicting transient flows of viscoplastic fluids. *J. Non-Newtonian Fluid Mech.* **287**, 104429.

Ahmadi, A., Olleik, H. & Karimfazli, I. 2022 Rayleigh–Bénard convection of carbopol microgels: Are viscoplastic models adequate? *J. Non-Newtonian Fluid Mech.* **300**, 104704.

Amanullah, A., Hjorth, S.A. & Nienow, A.W. 1998 A new mathematical model to predict cavern diameters in highly shear thinning, power law liquids using axial flow impellers. *Chem. Engng Sci.* **53** (3), 455–469.

Ameur, H. 2020 Newly modified curved-bladed impellers for process intensification: energy saving in the agitation of Hershel-Bulkley fluids. *Chem. Engng Process. Process Intensification* **154**, 108009.

Aref, H. 1984 Stirring by chaotic advection. *J. Fluid Mech.* **143**, 1–21.

Aref, H. *et al.* 2017 Frontiers of chaotic advection. *Rev. Mod. Phys.* **89** (2), 025007.

BALMFORTH, N.J., FRIGAARD, I.A. & OVARLEZ, G. 2014 Yielding to stress: recent developments in viscoplastic fluid mechanics. *Annu. Rev. Fluid Mech.* **46** (1), 121–146.

BARNES, H.A. 1999 The yield stress—a review or '$\pi\alpha\nu\tau\alpha\rho\varepsilon\iota$'—everything flows? *J. Non-Newtonian Fluid Mech.* **81** (1–2), 133–178.

BONN, D., DENN, M.M., BERTHIER, L., DIVOUX, T. & MANNEVILLE, S. 2017 Yield stress materials in soft condensed matter. *Rev. Mod. Phys.* **89** (3), 035005.

BOUJLEL, J., PIGEONNEAU, F., GOUILLART, E. & JOP, P. 2016 Rate of chaotic mixing in localized flows. *Phys. Rev. Fluids* **1** (3), 031301.

CAULFIELD, C.P. 2021 Layering, instabilities, and mixing in turbulent stratified flows. *Annu. Rev. Fluid Mech.* **53** (1), 113–145.

CHAPARIAN, E. & FRIGAARD, I.A. 2017*a* Cloaking: particles in a yield-stress fluid. *J. Non-Newtonian Fluid Mech.* **243**, 47–55.

CHAPARIAN, E. & FRIGAARD, I.A. 2017*b* Yield limit analysis of particle motion in a yield-stress fluid. *J. Fluid Mech.* **819**, 311–351.

CHRISTOV, C.I. & HOMSY, G.M. 2009 Enhancement of transport from drops by steady and modulated electric fields. *Phys. Fluids* **21** (8), 083102-1–083102-13.

COUSSOT, P. 2014 Yield stress fluid flows: a review of experimental data. *J. Non-Newtonian Fluid Mech.* **211**, 31–49.

DANESHVAR GARMROODI, M.R. & KARIMFAZLI, I. 2024 Mixing in heterogeneous fluids: an examination of fluid property variations. *J. Non-Newtonian Fluid Mech.* **325**, 105196.

DERKSEN, J.J. 2013 Simulations of mobilization of Bingham layers in a turbulently agitated tank. *J. Non-Newtonian Fluid Mech.* **191**, 25–34.

DIMOTAKIS, P.E. 2005 Turbulent mixing. *Annu. Rev. Fluid Mech.* **37** (1), 329–356.

DINKGREVE, M., PAREDES, J., DENN, M.M. & BONN, D. 2016 On different ways of measuring 'the' yield stress. *J. Non-Newtonian Fluid Mech.* **238**, 233–241.

DIVOUX, T., BARENTIN, C. & MANNEVILLE, S. 2011 From stress-induced fluidization processes to Herschel-Bulkley behaviour in simple yield stress fluids. *Soft Matt.* **7** (18), 8409–8418.

FAN, Y., PHAN-THIEN, N. & TANNER, R.I. 2001 Tangential flow and advective mixing of viscoplastic fluids between eccentric cylinders. *J. Fluid Mech.* **431**, 65–89.

FRIGAARD, I.A. & NOUAR, C. 2005 On the usage of viscosity regularisation methods for visco-plastic fluid flow computation. *J. Non-Newtonian Fluid Mech.* **127** (1), 1–26.

GALINDO, E., ARGÜELLO, M.A., VELASCO, D., ALBITER, V. & MARTÍNEZ, A. 1996 A comparison of cavern development in mixing a yield stress fluid by rushton and intermig impellers. *Chem. Engng Technol.* **19** (4), 315–323.

METZNER, A.B. & OTTO, R.E. 1957 Agitation of non-Newtonian fluids. *AIChE J.* **3** (1), 3–10.

MITSOULIS, E. & TSAMOPOULOS, J. 2017 Numerical simulations of complex yield-stress fluid flows. *Rheol. Acta* **56**, 231–258.

NIEDERKORN, T.C. & OTTINO, J.M. 1994 Chaotic mixing of shear-thinning fluids. *AIChE J.* **40** (11), 1782–1793.

OpenFOAM Foundation. OpenFOAM: Open source computational fluid dynamics toolbox. Available at: https://github.com/OpenFOAM.

OTTINO, J.M. 1989 *The Kinematics of Mixing: Stretching, Chaos, and Transport*, vol. 3. Cambridge University Press.

OTTINO, J.M. 1990 Mixing, chaotic advection, and turbulence. *Annu. Rev. Fluid Mech.* **22** (1), 207–254.

PAKZAD, L., EIN-MOZAFFARI, F., UPRETI, S.R. & LOHI, A. 2013 A novel and energy-efficient coaxial mixer for agitation of non-Newtonian fluids possessing yield stress. *Chem. Engng Sci.* **101**, 642–654.

PAUL, E.L., ATIEMO-OBENG, V.A. & KRESTA, S.M. 2004 *Handbook of Industrial Mixing: Science and Practice*. Wiley-Interscience.

PELTIER, W.R. & CAULFIELD, C.P. 2003 Mixing efficiency in stratified shear flows. *Annu. Rev. Fluid Mech.* **35** (1), 135–167.

PUTZ, A. & FRIGAARD, I.A. 2010 Creeping flow around particles in a Bingham fluid. *J. Non-Newtonian Fluid Mech.* **165** (5–6), 263–280.

ROSHKO, A. 1954 On the development of turbulent wakes from vortex streets. Tech. Rep.

SOLOMON, J., ELSON, T.P., NIENOW, A.W. & PACE, G.W. 1981 Cavern sizes in agitated fluids with a yield stress. *Chem. Engng Commun.* **11** (1–3), 143–164.

SOSSA-ECHEVERRIA, J. & TAGHIPOUR, F. 2015 Computational simulation of mixing flow of shear thinning non-Newtonian fluids with various impellers in a stirred tank. *Chem. Engng Process.* **93**, 66–78.

SPENCER, R.S. & WILEY, R.M. 1951 The mixing of very viscous liquids. *J. Colloid Sci.* **6** (2), 133–145.

SUPEKAR, R., HEWITT, D.R. & BALMFORTH, N.J. 2020 Translating and squirming cylinders in a viscoplastic fluid. *J. Fluid Mech.* **882**, A11.

TANGUY, P.A., BERTRAND, F., LABRIE, R. & BRITO-DE LA FUENTE, E. 1996 Numerical modelling of the mixing of viscoplastic slurries in a twin-blade planetary mixer. *Chem. Engng Res. Des.* **74** (4), 499–504.

TANNER, R.I. & MILTHORPE, J.F. 1983 Numerical simulation of the flow of fluids with yield stress. *Numer. Meth. Lam. Turbul. Flow Seattle* **64**, 680–690.

THOMPSON, R.L. & SOARES, E.J. 2016 Viscoplastic dimensionless numbers. *J. Non-Newtonian Fluid Mech.* **238**, 57–64.

TOKPAVI, D.L., JAY, P., MAGNIN, A. & JOSSIC, L. 2009 Experimental study of the very slow flow of a yield stress fluid around a circular cylinder. *J. Non-Newtonian Fluid Mech.* **164** (1–3), 35–44.

TOKPAVI, D.L., MAGNIN, A. & JAY, P. 2008 Very slow flow of Bingham viscoplastic fluid around a circular cylinder. *J. Non-Newtonian Fluid Mech.* **154** (1), 65–76.

UHL, V. 2012 *Mixing V1: Theory and Practice*. Elsevier.

VILLERMAUX, E. 2019 Mixing versus stirring. *Annu. Rev. Fluid Mech.* **51** (1), 245–273.

WACHS, A. & FRIGAARD, I.A. 2016 Particle settling in yield stress fluids: limiting time, distance and applications. *J. Non-Newtonian Fluid Mech.* **238**, 189–204.

WARHAFT, Z. 2000 Passive scalars in turbulent flows. *Annu. Rev. Fluid Mech.* **32** (1), 203–240.

WENDELL, D.M., PIGEONNEAU, F., GOUILLART, E. & JOP, P. 2013 Intermittent flow in yield-stress fluids slows down chaotic mixing. *Phys. Rev. E* **88** (2), 023024.

WHITCOMB, P.J. & MACOSKO, C.W. 1978 Rheology of xanthan gum. *J. Rheol.* **22** (5), 493–505.

WUNSCH, C. & FERRARI, R. 2004 Vertical mixing, energy, and the general circulation of the oceans. *Annu. Rev. Fluid Mech.* **36** (1), 281–314.